Emergence of nuclear clustering in electric-dipole excitations of ^{6}Li

S. Satsuka and W. Horiuchi
Department of Physics, Hokkaido University, Sapporo 060-0810, Japan

(Received 27 April 2019; published 29 August 2019)

Nuclear clustering plays an important role, especially in the dynamics of light nuclei. The importance of the emergence of the nuclear clustering was discussed in the recent measurement of the photoabsorption cross sections as it offered the possibility of the coexistence of various excitation modes which are closely related to the nuclear clustering. To understand the excitation mechanism, we study the electric-dipole ($E1$) responses of ^{6}Li with a fully microscopic six-body calculation. The ground-state wave function is accurately described with a superposition of correlated Gaussian (CG) functions with the aid of the stochastic variational method. The final-state wave functions are also expressed by a number of the CG functions including important configurations to describe the six-body continuum states excited by the $E1$ field. We found that the out-of-phase transitions occur due to the oscillations of the valence nucleons against the ^{4}He cluster at the low energies around 10 MeV indicating "soft" giant-dipole-resonance (GDR)-type excitations, which are very unique in the ^{6}Li system but could be found in other nuclear systems. At the high energies beyond ∼30 MeV typical GDR-type transitions occur. The ^{3}He-^{3}H clustering plays an important role to the GDR phenomena in the intermediate-energy regions around 20 MeV.

DOI: 10.1103/PhysRevC.100.024334

I. INTRODUCTION

Nuclear cluster structure often appears in the spectrum of light nuclei. Especially, the α(^{4}He) cluster plays a vital role to explain the low-lying spectra of $N = Z$ nuclei [1,2]. Much attention has been paid to the understanding of the role of nuclear clustering in the electromagnetic transitions of light nuclei, as their importance in the nucleosynthesis represented by the triple-α processes related to the famous Hoyle state in ^{12}C [3].

The electric-dipole ($E1$) transition strengths contain numerous information on the ground- and final-state wave functions and have often been used as a probe for the nuclear structure and dynamic properties. The giant dipole resonance (GDR) can be observed in any nuclear systems, which has been recognized as the classical picture of the out-of-phase oscillation between protons and neutrons induced by the $E1$ external field [4,5]. Since its resistance force stems from the nuclear saturation properties, the peak position, as well as its distributions, is closely related to the bulk properties of the nuclear matter, especially to the nuclear symmetry energy [6,7].

Recently, due to the new advancement of experimental techniques, exploration of new $E1$ excitation modes has attracted the interest of the nuclear physics community. In neutron-rich nuclei in which the neutron wave function is extended further than that of protons. In the low excitation energies the possibility of emerging the soft dipole excitation mode was pointed out as oscillations of a core against excess neutrons [8–11]. Recent microscopic calculations for halo nuclei showed that the low-lying $E1$ strengths have the typical soft-dipole type excitation character in ^{6}He [12–14] and ^{22}C [15]. Exotic excitations such as toroidal and compressive modes were also discussed in ^{10}Be as possible new excitations for light unstable nuclei [16].

Recently, the photoabsorption reaction cross sections of ^{6}Li were measured [17] in the energy range up to ∼60 MeV, where the $E1$ transitions are dominant. A two-peak structure in the photoabsorption cross sections was found and the peak at the lower and higher energies were respectively conjectured as the GDR of ^{6}Li and the GDR of the α cluster in ^{6}Li based on the idea given in the early study of the ^{6}Li(γ, n) reaction [18] for the interpretation of the higher peak. If this interpretation is true, then these kinds of subnuclear excitation modes may appear in various nuclear systems where the α-cluster structure is well developed.

In this paper, we study the $E1$ transitions of ^{6}Li. The ^{6}Li nucleus has often been described with an $\alpha + p + n$ three-body model (see, for example, Refs. [19–22] and references therein). However, to understand the $E1$ excitation mechanism of ^{6}Li, a fully microscopic six-body calculation is needed that can describe the formation and distortion of nuclear clusters in a wide range of the excitation energies up to ∼60 MeV. We calculate the $E1$ transition strengths and their transition densities and discuss how ^{6}Li is excited by the $E1$ field as a function of the excitation energy. We clarify the roles of light clusters in the $E1$ excitation spectrum extending the discussions given in Ref. [14]. In that paper, the proton-proton distance in the wave function of ^{6}He was introduced as a measure of the α clustering. However, it is not useful for the case of ^{6}Li because the wave function is totally antisymmetric with respect to the exchange of the nucleons and thus we cannot distinguish protons either in the α cluster or the valence part of ^{6}Li. Therefore, we calculate the spectroscopic factors of various cluster configurations as direct quantities of the clustering degrees of freedom.

The paper is organized as follows. In the next section, we define basic inputs used in the many-body variational

calculation. Section III explains details of the procedures to obtain the ground- and final-state wave functions for the six-nucleon system. In Sec. IV, we calculate the $E1$ transition strength distributions and discuss how the transition occurs as a function of the excitation energy by analyzing their transition densities focusing on the roles of the nuclear clustering. The compressive isoscalar dipole strengths are also evaluated as they reflect the other profiles of the transition densities. Conclusions are made in Sec. V. In the Appendices, we give details of the evaluation of the spectroscopic factors and complementary analyses for the nuclear clustering in the $E1$ transitions.

II. MICROSCOPIC FEW-NUCLEON MODEL

Here we briefly describe the microscopic few-nucleon model employed in this paper. The Hamiltonian for an N-nucleon system consists of the kinetic energy and two-body potential terms V_{ij} as

$$H = \sum_{i=1}^{N} T_i - T_{\rm c.m.} + \sum_{i>j} V_{ij}, \tag{1}$$

where T_i is the kinetic energy of the ith nucleon. The center-of-mass (c.m.) kinetic energy $T_{\rm c.m.}$ is properly subtracted, and hence no spurious $E1$ excitation appears in the calculation. As a nucleon-nucleon potential, we employ an effective central potential, the Minnesota (MN) potential [23], which offers a fair description of the binding energies and radii of s-shell nuclei, ^{2}H (d), ^{3}H (t), ^{3}He (h), and ^{4}He (α) [24,25] without a three-body force. For a more quantitative discussion, we need to use realistic nucleon-nucleon and three-nucleon forces. However, this is too involved for the complicated six-body system. As shown in Refs. [26,27], the central effective force also give a fair description of the photoabsorption reactions for the s-shell nuclei. For the sake of simplicity, in this paper, we use the MN potential that drastically reduces the computational costs. The MN potential includes the one parameter u that controls the strength of the odd-parity waves. Later we will discuss how to choose the u parameter. The Coulomb interaction is also included.

The N-nucleon wave function with spin J and its projection M_J are expanded in terms of the fully antisymmetrized basis function $\Phi^{(N)}_{JM_J,i}$

$$\Psi^{(N)}_{JM_J} = \sum_{i=1}^{K} C^{(N)}_i \Phi^{(N)}_{JM_J,i}. \tag{2}$$

For the basis function, we employ the global vector representation of the correlated Gaussian basis function [24,28] as

$$\Phi^{(N)}_{JM_J,i} = \mathcal{A}\Big\{ \exp\left(-\tfrac{1}{2}\tilde{\boldsymbol{x}}A_i\boldsymbol{x}\right)\left[\mathcal{Y}_{L_i}(\tilde{v}_i\boldsymbol{x})\chi^{(N)}_{S_i}\right]_{JM_J}\eta^{(N)}_{M_T}\Big\}, \tag{3}$$

where $\mathcal{A}$ is the antisymmetrizer. As the coordinate set $\boldsymbol{x} = (\boldsymbol{x}_1, \ldots, \boldsymbol{x}_{N-1})^t$ excluding the center-of-mass coordinate of the N-nucleon system, $\boldsymbol{x}_N$, we conveniently take it as the Jacobi coordinate set: $\boldsymbol{x}_k = \boldsymbol{r}_{k+1} - \boldsymbol{x}^{(k)}_{\rm c.m.}$ with the center-of-mass coordinate of the k-nucleon subsystem, $\boldsymbol{x}^{(k)}_{\rm c.m.} = \sum_{j=1}^{k} \boldsymbol{r}_j/k$. A tilde denotes the transpose of a matrix. The matrix A is an $(N-1)$-dimensional positive-definite symmetric matrix. The correlations among the particles are explicitly described through the off-diagonal matrix elements of A, noting that a quadratic form $\tilde{\boldsymbol{x}}A\boldsymbol{x} = \sum_{jk} A_{jk}\boldsymbol{x}_j \cdot \boldsymbol{x}_k$ on the exponent. The rotational motion of the system is described with the so-called global vector $\tilde{v}\boldsymbol{x} = \sum_{j=1}^{N-1} v_j \boldsymbol{x}_j$ [28,29]. Because the functional form does not change under any linear transformation of the coordinate, the form of Eq. (3) is convenient to include various configurations such as single-particle $\alpha + p + n$ and $h + t$ cluster configurations as described in Sec. III B. With this nice property, the correlated Gaussian method has been applied to many examples related to nuclear clustering. The readers are referred to various applications [30–32] and review papers [33,34].

The N-nucleon spin function with the total spin S and its projection M_S is given as the successive coupling of N single-particle spin functions $\chi_{\frac{1}{2}m_s}$ as

$$\chi^{(N)}_{SM_S} = \left[\ldots\left[\left[\chi_{\frac{1}{2}}(1)\chi_{\frac{1}{2}}(2)\right]_{S_{12}}\chi_{\frac{1}{2}}(3)\right]_{S_{123}}\ldots\right]_{SM_S}. \tag{4}$$

All possible intermediate spins $S_{12}, S_{123}, \ldots, S_{123\cdots N-1}$ are taken into account in the calculation. The isospin function with the total isospin T and its projection $M_T = \sum_{j=1}^{N} m_{t_j}$ is represented by the particle basis which is the direct product of N single-particle isospin functions $\eta_{\frac{1}{2}m_t}$ as

$$\eta^{(N)}_{M_T} = \eta_{\frac{1}{2}m_{t_1}}(1)\cdots\eta_{\frac{1}{2}m_{t_N}}(N) \tag{5}$$

with $m_{t_j} = 1/2$ for neutron and $-1/2$ for proton. In the particle basis, the mixture of possible total isospin states with, e.g., $T = 0$, 1, 2, and 3 for ^{6}Li, is naturally taken into account.

After those parameters of the basis functions are set, we determine the K-dimensional coefficient vector $\boldsymbol{C} = [C^{(N)}_1, \ldots, C^{(N)}_K]^t$ by solving the generalized eigenvalue problem

$$H\boldsymbol{C} = EB\boldsymbol{C} \tag{6}$$

with $B_{ij} = \langle\Phi^{(N)}_{JM_J,i}|\Phi^{(N)}_{JM_J,j}\rangle$ and $H_{ij} = \langle\Phi^{(N)}_{JM_J,i}|H|\Phi^{(N)}_{JM_J,j}\rangle$. These matrix elements can be evaluated analytically. See Refs. [24,25,28] for the detailed mathematical derivation and expressions.

III. CALCULATIONS OF THE WAVE FUNCTIONS

In this paper, we mainly discuss the $E1$ transitions. The reduced $E1$ transition probabilities or $E1$ transition strengths are defined by

$$B(E1, E_f) = \frac{1}{2J_0+1}\sum_{J_fM_fM_0\mu}\left|\left\langle\Psi^{(N)}_{J_fM_f}(E_f)\right|\right. \times \left.\mathcal{M}(E1,\mu)\left|\Psi^{(N)}_{J_0M_0}(E_0)\right\rangle\right|^2 \tag{7}$$

with the $E1$ operator

$$\mathcal{M}(E1,\mu) = e\sqrt{\frac{4\pi}{3}}\sum_{i\in p}^{N}\mathcal{Y}_{1\mu}(\boldsymbol{r}_i - \boldsymbol{x}_N) \tag{8}$$

with a solid spherical harmonic, $\mathcal{Y}_{\lambda\mu}(\boldsymbol{r}) = r^\lambda Y_{\lambda\mu}(\hat{\boldsymbol{r}})$, where the summation i runs only for proton. In this section, we describe detailed setup of the calculations for the initial-ground-

TABLE I. Ground-state properties of ^{6}Li. Energy and radii are given in units of MeV and fm, respectively. See text for details. The experimental data are taken from Refs. [35,36].

u	$E_0(^6\mathrm{Li})$	$E_0(\alpha)$	S_{pn}	r_m	r_p	r_n	r_{pp}	$S^2_{\alpha d}$
1.00	−34.63	−29.94	4.7	2.20	2.20	2.20	3.62	0.856
0.93	−33.63	−29.90	3.7	2.33	2.34	2.33	3.86	0.869
0.87	−32.94	−29.87	3.1	2.45	2.46	2.45	4.07	0.882
Expt.	−31.99	−28.30	3.70		2.452			

state and final-continuum-state wave functions, $\Psi_{J_0M_0}(E_0)$ and $\Psi_{J_fM_f}(E_f)$, respectively.

A. Ground-state wave functions

For the ground-state wave function with the total angular momentum and parity $J^\pi = 1^+$, in this paper, we consider only the total orbital angular momentum $L = 0$ with the total spin $S = 1$ state because the MN potential does not mix with the higher-angular-momentum states. It does not mean that the particles are not correlated. Higher partial waves for all relative coordinates are taken into account through the off-diagonal matrix elements of the matrix A of Eq. (3) in the optimization procedure explained below.

As mentioned in the previous section, we need to optimize a huge number of the variational parameters. To achieve it efficiently, we employ the stochastic variational method (SVM) [24,28]. First, we adopt the competitive selection from randomly selected candidates and increase the basis size until a certain number of basis states is obtained with $u = 1.00$. Then we switch the selection procedure for the refinement of the variational parameters in the already-obtained basis functions until the energy is converged within tens of keV. The convergence is reached at $K = 600$ in Eq. (2) as adopted in Ref. [14]. This number is very small by noting that the matrix A includes $N(N-1)/2$ parameters as well as the spin degrees of freedom for each basis function. For the wave functions with other u parameters, we start with the optimal basis functions with $u = 1.00$ and refine those basis functions by keeping the total number of basis unchanged until the energy convergence is reached.

Table I lists the ground-state properties of ^{6}Li with different values of the u parameter in the MN potential. As shown in the binding energy of ^{6}Li, $E_0(^6\mathrm{Li})$, the original MN potential ($u = 1.00$) offers slightly strong odd-wave interaction to reproduce the two-nucleon separation energy of ^{6}Li, S_{pn}, leading to the small rms point-proton radius, r_p, compared to the measurement [36]. It is noted that the u parameter does not affect the interaction for the even-parity partial waves but only for the odd-parity ones. Roughly speaking, the u parameter controls the interaction of the valence nucleons from the α core on the p-shell orbital. In fact, as listed in Table I, the binding energies of the α particle, $E_0(\alpha)$, have almost no dependence on u. Therefore, we prepare two more sets by considering the repulsive odd-wave strength: One set is to reproduce the experimental S_{pn} value ($u = 0.93$), and the other set reproduces the experimental r_p value ($u = 0.87$).

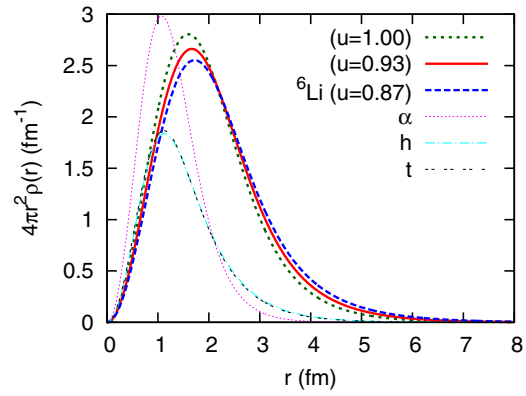

FIG. 1. Point-matter densities of ^{6}Li with different values of the u parameter in the MN potential. The densities of α, h, and t with $u = 0.93$ are also plotted for comparison.

As shown in the table, the smaller the S_{pn} value, the larger the nuclear radii becomes. The small difference between r_p and the rms point-neutron radius, r_n, is due to the Coulomb interaction, which is described in this study. The proton-proton distance, r_{pp}, is also calculated and listed in the table for the sum-rule evaluation given in Appendix C.

Figure 1 plots the point-matter densities of ^{6}Li with different values of the u parameter. The nuclear surface slightly extends with decreasing the odd-wave strength or the u parameter. Peak positions are located in the range 1.6–1.7 fm and their magnitude becomes half at about 2.7–2.8 fm. We also plot the densities of α, h, and t with $u = 0.93$. The calculated binding energies of h and t are respectively −7.68 and −8.38 MeV for $u = 1.00$. They also do not depend on the choice of the u parameter. Only a 0.01-MeV difference is obtained for decreasing u to 0.93 and 0.87. The peak of the density of α is at about 1 fm, showing the sharper distribution as compared to that of ^{6}Li. The peak position of h and t are almost the same as that of ^{4}He but the half-density positions are somewhat larger than that of ^{4}He due to the weaker binding.

The ^{6}Li nucleus is known to have developed α cluster structure and is well described with an $\alpha + p + n$ three-body model [21] having a significant amount of the $\alpha + d$ component [22,37]. As a measure of the clustering degrees of freedom, we also show the spectroscopic factor of the $\alpha + d$ configuration. The probability of finding the two-cluster (a and b) configurations in the ^{6}Li wave function is defined by

$$S^2_{ab} = \left|\left\langle \Psi^{(a)}\Psi^{(b)} \middle| \Psi^{(6)}_{JM_J}(E)\right\rangle\right|^2, \tag{9}$$

where $\Psi^{(a)}$, $\Psi^{(b)}$, and $\Psi^{(6)}_{JM_J}(E)$ are the ground-state wave functions of nuclei a, b, and ^{6}Li with energy E, respectively. The relative wave function on the coordinate between the center of mass of the nuclei a and b is integrated out. Details of this evaluation are given in Appendix A. We calculate the $S^2_{\alpha d}$ values ($a = \alpha$, $b = d$) for the ground-state wave functions, which are listed in Table I. The $S^2_{\alpha d}$ values are large (0.86–0.88) for all the values of the u parameter, which is consistent with the value obtained with the variational Monte Carlo

calculation, 0.84 [38]. The $\alpha + d$ cluster structure is somewhat distorted by the NN interaction and the Pauli principle. In fact, the $S^2_{\alpha d}$ value slightly increases by adding the repulsive α-nucleon interaction with $u = 0.93$ and 0.87. Though $S^2_{\alpha d}$ values are large, no bound state in the ^{6}Li system is obtained only with the $\alpha + d$ configurations with a relative s-wave. Inclusion of those distorted configurations is essential to get binding in the six-nucleon system.

B. Final-state wave functions

In this subsection, we explain how to construct the final-state wave functions excited by the $E1$ operator. We follow almost the same prescription as given in Refs. [14,39,40] but extended to adapt it to the ^{6}Li case. The ground-state wave function with $J^\pi = 1^+$ is excited by the $E1$ operator. Since the operator does not change the spin of the initial state $S = 1$, the orbital angular momentum of the final state should be $L = 1$ and thus the $J^\pi = 0^-, 1^-$, and 2^- states need to be considered. In this paper, we did not include the spin-orbit interaction. These states are energetically degenerate; only its multipolarity is different.

We expand the final-state wave function in a large number of the correlated Gaussian basis functions of Eq. (3). To incorporate the complicated six-body correlations efficiently, physically important configurations are selected and categorized into three types: (I) single-particle (sp) excitation, (II) $4 + 1 + 1$ cluster, and (III) $3 + 3$ cluster configurations. All these configurations are again expressed by the same functional form as in Eq. (3) with appropriate coordinate transformations.

The configurations of type (I) is based on the idea that the $E1$ operator excites one coordinate in the ground-state wave function and these configurations are further subcategorized into three channels which will be explained later in this paragraph. The resulting coherent states are important to satisfy the $E1$ sum rule [39]. The configurations of type (I) are constructed by using the basis set of the ground-state wave function of ^{6}Li by multiplying additional angular momentum $L = 1$ as

$$\Phi^{(\mathrm{sp},m)}_{JM_J,i} = \mathcal{A}\big[\Phi^{(6)}_{1,i}(123456)\mathcal{Y}_1\big(\boldsymbol{r}_1 - \boldsymbol{x}^{(m)}_{\mathrm{c.m.}}\big)\big]_{JM_J}, \tag{10}$$

where $\Phi^{(6)}_{1,i}$ is the ith basis ($i = 1, \ldots, 600$) of the ground-state wave function of ^{6}Li. The coordinate $\boldsymbol{r}_1$ denotes the single-particle coordinate of a proton. As a first choice, we take the coordinate of one proton measured from the center of mass of the system ($m = 6$). Considering that ^{6}Li has a large $S^2_{\alpha d}$ component ($\sim$0.9), we include the additional sp basis sets that the four- and two-nucleon subsystems are excited by the $E1$ operator (the channels with $m = 4$ and 2). Finally, the total number of the basis of the type (I) is 1800 including the channels with $m = 6$, 4, and 2.

The configurations of types (II) and (III) explicitly take care of the cluster configurations of $\alpha + p + n$ and $h + t$, which correspond to the two lowest thresholds, 3.7 and 15.8 MeV [35], respectively. They are expected to be important for describing the low-lying ($\lesssim$16 MeV) and intermediate energies ($\gtrsim$16 MeV).

The configurations of type (II) are defined in the following:

$$\Phi^{(411,l)}_{JM_J,ijk} = \mathcal{A}\big\{\Phi^{(4)}_{0,i}(1234)\exp\big[-\tfrac{1}{2}\tilde{\boldsymbol{y}}B^{(jk)}\boldsymbol{y}\big]\big[\mathcal{Y}_l\big(\boldsymbol{y}^{(\mathrm{X})}_l\big)\times\big[\chi_{\frac{1}{2}}(5)\chi_{\frac{1}{2}}(6)\big]_{S_{56}}\big]_{JM_J}\eta_{\frac{1}{2},-\frac{1}{2}}(5)\eta_{\frac{1}{2},\frac{1}{2}}(6)\big\}, \tag{11}$$

where $\Phi^{(4)}_{0,i}$ is the ith basis that gives the ground-state energy of ^{4}He with the full set of these basis functions. The following two types of relative coordinates are considered:

(i) Y-type

$$\boldsymbol{y}^{(\mathrm{Y})}_1 = \boldsymbol{r}_5 - \boldsymbol{x}^{(4)}_{\mathrm{c.m.}}, \quad \boldsymbol{y}^{(\mathrm{Y})}_2 = \boldsymbol{r}_6 - \frac{\boldsymbol{r}_5 + 4\boldsymbol{x}^{(4)}_{\mathrm{c.m.}}}{5}, \tag{12}$$

(ii) T-type

$$\boldsymbol{y}^{(\mathrm{T})}_1 = \boldsymbol{r}_6 - \boldsymbol{r}_5, \quad \boldsymbol{y}^{(\mathrm{T})}_2 = \frac{\boldsymbol{r}_5 + \boldsymbol{r}_6}{2} - \boldsymbol{x}^{(4)}_{\mathrm{c.m.}}. \tag{13}$$

These configurations are essential for describing the two valence nucleon motion around the α core, which will be important, especially, in the low-lying energies. For the Y-(T-)type channel, we assume that both of the $\boldsymbol{y}^{(\mathrm{X})}_1$ and $\boldsymbol{y}^{(\mathrm{X})}_2$ coordinates are initially in p (s) wave and the one coordinate is excited to the s- (p-) wave state. We consider that either $\boldsymbol{y}^{(\mathrm{X})}_1$ or $\boldsymbol{y}^{(\mathrm{X})}_2$ in each coordinate set is excited by the $E1$ operator, that is, the basis set with $l = 1$ and 2 are independently included respectively for (i) and (ii). The relative wave functions of the valence nucleons are expanded with several Gaussian functions covering short to far distances, that is, the diagonal matrix elements of a 2×2 matrix B, e.g., $B_{11} = 1/b^2_{11}$, are chosen by a geometric progression with 18 and 15 basis ranging from 0.1 to 22 fm for the $\boldsymbol{y}^{(\mathrm{X})}_1$ and $\boldsymbol{y}^{(\mathrm{X})}_2$ coordinates, respectively. For practical computations, we truncate the number of the basis function of the four-nucleon subsystem, $\Phi^{(4)}_{0,i}$, with 15 bases. Though the energy loss of this α particle is tiny, in which only a 0.3-MeV difference from the full model space calculation is found, it drastically reduces the total number of basis functions.

The configurations of type (III) are defined as

$$\Phi^{(33)}_{JM_J,ijk} = \mathcal{A}\big\{\big[\big[\Phi^{(3)}_{\frac{1}{2},i}(123)\Phi^{(3)}_{\frac{1}{2},j}(456)\big]_{J_3}\times\exp\big(-\tfrac{1}{2}b_k z^2\big)\mathcal{Y}_1(z)\big]_{JM_J}\big\} \tag{14}$$

with

$$z = \frac{\boldsymbol{r}_1 + \boldsymbol{r}_2 + \boldsymbol{r}_3}{3} - \frac{\boldsymbol{r}_4 + \boldsymbol{r}_5 + \boldsymbol{r}_6}{3}, \tag{15}$$

where $\Phi^{(3)}_{\frac{1}{2},i}(123)$ and $\Phi^{(3)}_{\frac{1}{2},j}(456)$ are the ith and jth bases that give respectively the ground-state energies of ^{3}He and ^{3}H with the full set of these basis functions. These configurations describe the model space that directly excites the $h + t$ cluster degrees-of-freedom imprinted on the ground-wave function of ^{6}Li ($S^2_{ht} \approx 0.4$). The relative wave function for the coordinate z is expanded by 10 Gaussian functions with p wave to reduce the computational cost. We also truncate the total number of basis functions for the three-nucleon subsystems by seven bases resulting in only 0.2-MeV energy loss in these h and t particles.

Figure 2 shows schematic figures of the sets of the basis functions explained above. Circles and the red thick line indicate the protons and the coordinate excited by the $E1$

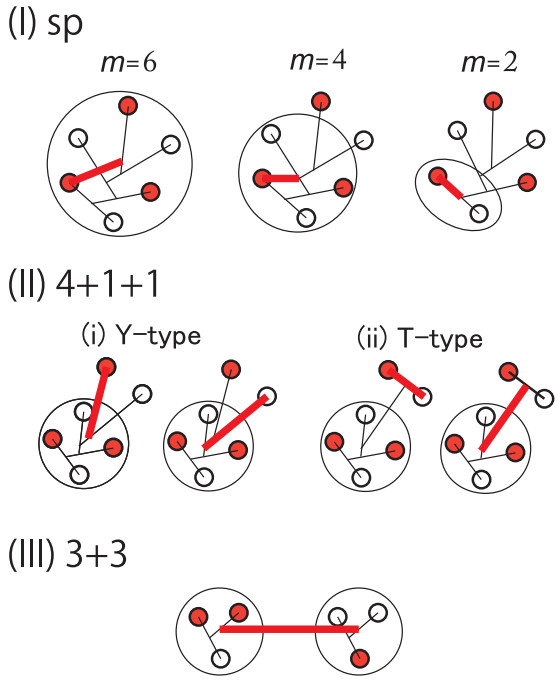

FIG. 2. Schematic figures of the basis functions for the final-state wave functions. Colored and uncolored small circles represent protons and neutrons, respectively. Thick lines indicate the coordinates excited by the $E1$ operator. See text for exact definitions.

operator, respectively. Note that we include all the basis states for each subsystem independently. The final-state wave functions are not restricted, as the subsystems are the ground state, but the excitations and distortion of ^{6}Li, α, h, and t are included through the coupling of the pseudoexcited states of those nuclear systems. The number of bases included in this calculation is 1800, 16 200, and 490 for the configurations of types (I), (II), and (III), respectively. We diagonalize the Hamiltonian, including all the configurations with 18 490 basis functions, and find $\sim 2 \times 10^3$ states below the excitation energy of 100 MeV.

IV. RESULTS AND DISCUSSIONS

A. Electric-dipole transitions and nuclear clustering

Figure 3 plots the $E1$ transition strengths obtained with the full model space that includes the configurations of types (I)–(III) described in the previous section with different values of the u parameter as a function of the excitation energy, $E_x = E_f - E_0$. For all these u values, we see several large $B(E1)$ values in the low- ($E_x \lesssim 16$ MeV), intermediate- ($E_x \approx 16$–30 MeV), and high- ($E_x \gtrsim 30$ MeV) energy regions. Though there is little quantitative difference among these three different cases up to $E_x \approx 40$ MeV, hereafter we discuss the results with $u = 0.93$ unless otherwise mentioned.

The structure of those peaks becomes more transparent by categorizing those states with respect to the spectroscopic factors of the $\alpha + p + n$ configuration,

$$S^2_{\alpha pn} = \left| \left\langle \Psi^{(\alpha)} \Psi^{(p)} \Psi^{(n)} \middle| \Psi^{(6)}_{JM_J}(E) \right\rangle \right|^2, \tag{16}$$

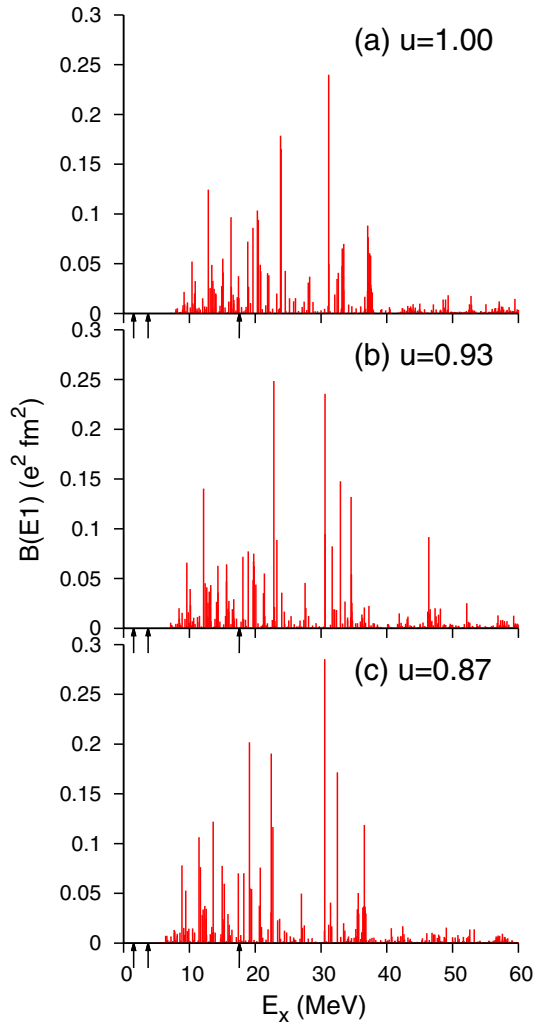

FIG. 3. Electric-dipole strengths of ^{6}Li with the full model space with (a) $u = 1.00$, (b) 0.93, and (c) 0.87. Arrows indicate the theoretical $\alpha + d$, $\alpha + p + n$, and $h + t$ thresholds from left to right, respectively.

where $\Psi^{(\alpha)}$ is the ground-state wave function of ^{4}He, and $\Psi^{(p)}$ ($\Psi^{(n)}$) is the proton (neutron) wave function. All the relative coordinates between clusters, spins and isospins are integrated out. Details about the evaluation are given in Appendix A. Note that $S^2_{\alpha d}$ is a subset of $S^2_{\alpha pn}$ but the states with large $S^2_{\alpha d}$ value do not contribute to the $E1$ transition. No $E1$ transition occurs from the ground state to those states because their total isospins are almost 0.

Figure 4(a) displays the transition strengths to the states with $S^2_{\alpha pn} > 0.80$. We find that the $E1$ transition strengths distribute in ranges from 10 to 40 MeV and that most of the low-lying states below 20 MeV have a large $\alpha + p + n$ cluster component, which is consistent by reminding the facts that the lowest $h + t$ threshold is 15.8 MeV [35].

Figure 4(b) shows the $E1$ strengths with $S^2_{ht} > 0.50$. Three large $E1$ strengths appear after the $h + t$ threshold opens. We find that these peak structures are robust, and their positions and strengths do not depend much on the values of the u parameter. The first two structures may correspond to the

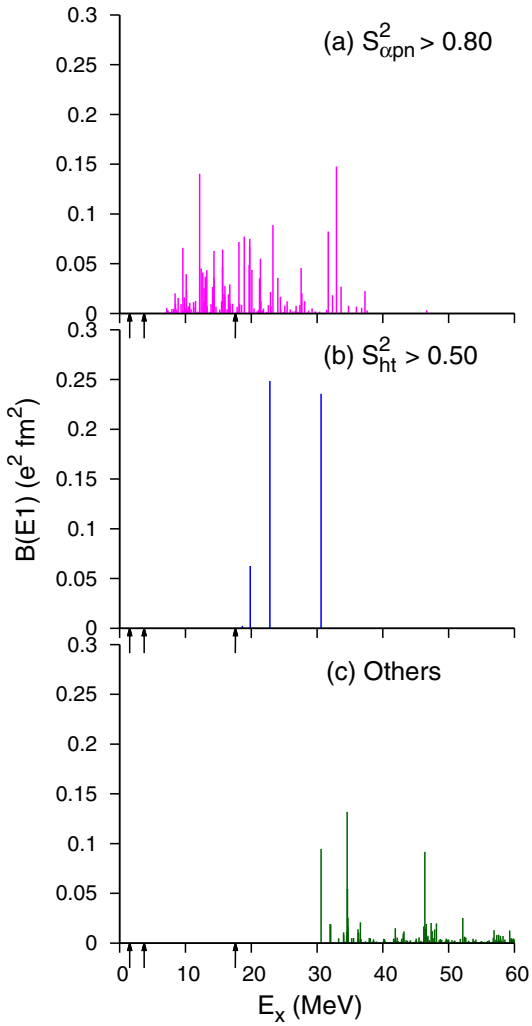

FIG. 4. Electric-dipole strengths of ^{6}Li with the full model space with $u = 0.93$ categorized by the amount of the spectroscopic factors into three: (a) $S^2_{\alpha pn} > 0.80$, (b) $S^2_{ht} > 0.5$, and (c) neither (a) nor (b). See text for details. Arrows indicate the theoretical $\alpha + d, \alpha + p + n$, and $h + t$ thresholds from left to right, respectively.

observed $J^\pi = 2^-$ levels at $E_x = 17.98$ and 26.59 MeV with the $h + t$ decay widths of 3.0 and 8.7 MeV, respectively [35].

The other strengths, which cannot be categorized into the above two conditions, are plotted in Fig. 4(c). They appear beyond 30 MeV and some prominent $E1$ strengths are found between 30 and 40 MeV. In this energy region, all the particle thresholds are open. Various configurations can couple with each other. We will discuss more details in Sec. IV B.

We discuss the structure of the states with large $E1$ strengths. For quantitative discussions, we list, in Table II, E_x, $B(E1)$, $S^2_{\alpha pn}$, and S^2_{ht} of the states giving the four largest $B(E1)$ values in the low-, intermediate-, and high-energy regions with $u = 0.93$. In the low-energy regions ($E_x \lesssim 16$ MeV) below the $h + t$ threshold, all the states have large $S^2_{\alpha pn}$ values, being almost unity, whereas their S^2_{ht} values are almost zero.

In the intermediate-energy regions around 20 MeV where it is energetically possible that the α cluster can break, although most of the states still have large $S^2_{\alpha pn}$ values, the state at

TABLE II. Excitation energy (E_x), reduced electric-dipole transition probability [$B(E1)$] in unit of e^2fm^2, and $\alpha + p + n$ ($S^2_{\alpha pn}$) and $h + t$ (S^2_{ht}) spectroscopic factors of ^{6}Li with $u = 0.93$. Note that two prominent strengths with different configurations appear at $E_x = 30.6$ MeV.

E_x (MeV)	$B(E1)$	$S^2_{\alpha pn}$	S^2_{ht}
9.6	0.066	0.999	0.000
12.1	0.140	0.999	0.011
14.3	0.063	0.997	0.000
15.7	0.064	0.999	0.010
18.9	0.077	0.991	0.004
19.8	0.075	0.994	0.003
22.8	0.249	0.113	0.850
23.3	0.089	0.963	0.003
30.6	0.236	0.264	0.533
30.6	0.095	0.780	0.158
33.0	0.148	0.962	0.005
34.6	0.132	0.195	0.019

$E_x = 22.8$ MeV has a small $S^2_{\alpha pn}$ value in which the α cluster in the six-nucleon system is strongly distorted. This state is dominated by the $h + t$ configuration having a large S^2_{ht} value, 0.850.

In the high-energy regions beyond ~30 MeV where all the particle thresholds are open, various structures are found: a mixture of $\alpha + p + n$ and $h + t$ components at $E_x = 30.6$ MeV, an almost pure $\alpha + p + n$ component at $E_x = 33.0$ MeV, and neither $\alpha + p + n$ nor $h + t$ components at $E_x = 34.6$ MeV.

We have shown the $E1$ strength distributions with the full model space including the breaking and polarization of the clusters in ^{6}Li. To make the role of these effects clearer, we discuss the $E1$ transition strengths only with the $\alpha + p + n$ and $h + t$ configurations in Appendix B and the impact of the clustering configurations on the $E1$ sum rule in Appendix C.

B. Structure of the electric-dipole excitation

Let us discuss the spatial structure of the $E1$ transitions. For this purpose, we calculate the transition densities of ^{6}Li for the analysis of the $E1$ transition mode [14],

$$\rho^{\rm tr}_{p/n}(r) = \sum_{i\in p/n} \left\langle \Psi^{(6)}_{J_f} \middle\| \mathcal{Y}_1(\boldsymbol{r}_i - \boldsymbol{x}_6)\delta(|\boldsymbol{r}_i - \boldsymbol{x}_6| - r) \middle\| \Psi^{(6)}_{J_0} \right\rangle, \tag{17}$$

for proton and neutron. These quantities represent the spatial distributions of the proton and neutron transition matrices and we note that the $E1$ transition matrix can be obtained with

$$\left\langle \Psi^{(6)}_{J_f} \middle\| \mathcal{M}(E1) \middle\| \Psi^{(6)}_{J_0} \right\rangle = e\sqrt{\frac{4\pi}{3}} \int_0^\infty dr\, \rho^{\rm tr}_p(r). \tag{18}$$

We discuss the transition densities of ^{6}Li to the selected states that show some characteristic behaviors. Figure 5 plots the transition densities for proton and neutron that correspond to the prominent $B(E1)$ peaks with $B(E1) > 0.1\ e^2\,\text{fm}^2$. At the low-energy (a) $E_x = 12.1$ MeV, we see the in-phase

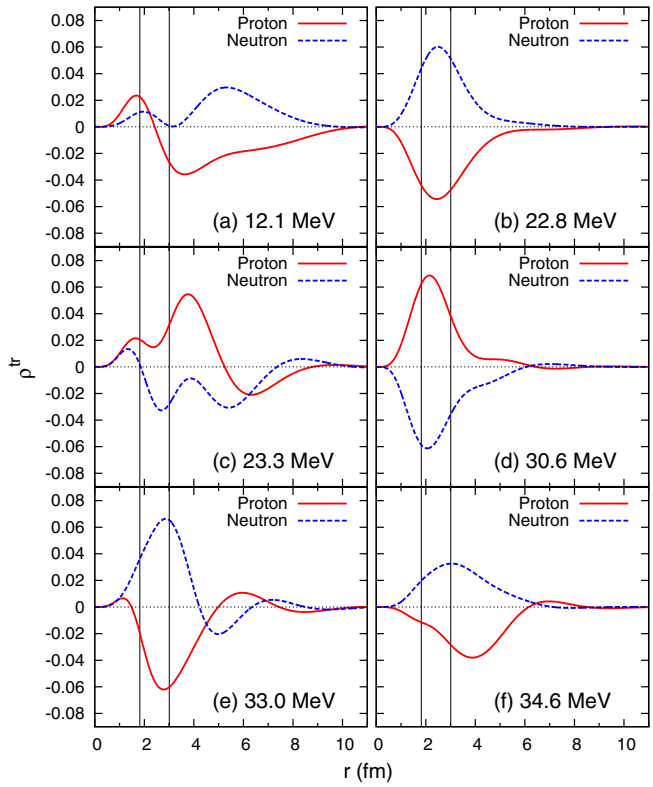

FIG. 5. Transition densities of ^{6}Li with the excitation energy of (a) 12.1, (b) 22.8, (c) 23.3, (d) 30.6, (e) 33.0, and (f) 34.6 MeV selected from Table II. See text for details. Note that left panels plot the transition densities with the states having large $S^2_{\alpha pn} \approx 1$. Vertical thin lines indicate theoretical nuclear radii, $\sqrt{\frac{5}{3}} r_m$, with $r_m = 1.41$ and 2.33 fm for ^{4}He and ^{6}Li, respectively.

transition below the ^{6}Li radius and the out-of-phase transitions occur outside the nuclear surface. This characteristic transition can be interpreted as the GDR-like or Goldhaber-Teller-(GT) dipole-type oscillation [4] of the valence proton and neutron around the core (α). In fact, the state has a large $S^2_{\alpha pn}$ value, as listed in Table II. This type of "soft" GT-dipole mode is very unique in ^{6}Li and differs from the soft-dipole mode expected in ^{6}He because of the oscillation between the valence two neutrons against the core. We note that the $E1$ transitions to $\alpha + d$ is almost forbidden because the $E1$ operator is isovector and the ground state of ^{6}Li is an almost-pure $T = 0$ state though a small mixture of the other total isospin states is included. Actually, the $S^2_{\alpha d}$ value for this state is 0.02. Studying the low-lying $E1$ excitations of ^{6}Li is the ideal example that the soft GT-dipole mode dominates.

In the energy regions where the $h + t$ threshold opens, we see clear out-of-phase transitions in all regions at (b) $E_x = 22.8$ MeV, which is typical for the GDR mode. As S^2_{ht} is large >0.8, this behavior comes from the $E1$ excitation of the relative motion between the h and t clusters. Peak positions are at $\sim$2 fm located at the sum of the peak positions of the density distributions of ^{3}H and ^{3}He displayed in Fig. 1. Such cluster GT-dipole modes can appear in any nuclear system but its emergence depends on the location of the cluster threshold. In light nuclei, since the cluster threshold becomes low, the cluster GT dipole modes can appear in the lower-lying regions. For the ^{7}Li case, the $\alpha + t$ threshold is lowest (2.47 MeV [35]; it differs from the case of ^{6}Li), and the cluster GT-dipole mode is expected to appear in the lowest-energy regions.

We also find large $B(E1)$ value at almost the same energy (c) $E_x = 23.3$ MeV. Similarly to the transition density at (a) $E_x = 12.1$ MeV, we see the in-phase transition below the ^{6}Li radius, but more oscillations in the out-of-phase transition appear in the outside of the nuclear surface. Since this state has large $S^2_{\alpha pn}$ values, as listed in Table II, this state can be interpreted as a vibrational excitation of the soft GT-dipole mode. The transition densities with (e) $E_x = 33.0$ shows the similar character having more oscillations.

At (d) $E_x = 30.6$ MeV, this shows the out-of-phase transition in all regions. Since the peak position is almost the same as that of (b) $E_x = 23.3$ MeV and has large mixture of $h + t$ configurations, $\sim$0.5, listed in Table II, this state can be regarded as a vibrational excitation of the state with (c) $E_x = 23.3$ MeV which exhibits $h + t$ clustering.

Finally, the state with (f) $E_x = 34.6$ MeV shows also the out-of-phase transition in all regions but the peak positions are located outside of the nuclear surface showing totally different structure from that of the $h + t$ oscillation. Neither $S^2_{\alpha pn}$ nor S^2_{ht} is large, as listed in Table II. This state can be regarded as having the typical GDR structure where the protons and neutrons oscillate opposite to each other [4].

To strengthen the interpretations given above, we present the transition densities with the final-state wave functions only with the $\alpha + p + n$ and $h + t$ configurations in Appendix B.

In summary, various types of the $E1$ excitations of ^{6}Li can be classified by focusing on nuclear clustering. Figures 5(a), 5(c) and 5(e) have the same characteristics whereby the in-phase transition below the ^{6}Li radius is due to α clustering and out-of-phase transitions of the valence nucleons beyond the nuclear surface (Soft GT-dipole mode). Figures 5(b), 5(d) and 5(f) show the out-of-phase transition in all regions. The excitation modes of Figs. 5(b) and 5(d) originate from the oscillations between the h and t clusters (Cluster GT-dipole mode), and Fig. 5(f) is the typical GDR oscillation where protons and neutrons oscillate opposite to each other (GT-dipole mode).

C. Photoabsorption cross sections

The total photoabsorption cross section is calculated by using the formula [41]

$$\sigma_\gamma(E_\gamma) = \frac{4\pi^2}{\hbar c} E_\gamma \frac{1}{3} \frac{dB(E1, E_\gamma)}{dE}. \quad (19)$$

The continuum states are discretized in this calculation. For a practical reason, they are often smeared by the Lorentzian functions $dB(E1,E)/dE = \frac{\Gamma}{2\pi} \sum_\nu B(E1, E_\nu)/[(E - E_\nu - E_0)^2 + (\Gamma/2)^2]$, using a certain Γ value as a free parameter [42]. To compare with the recent experiment, we fix the width parameter to reproduce the total sum of the experimental cross sections of Ref. [17]. However, the energy-independent width does not work, which results in the unphysically large

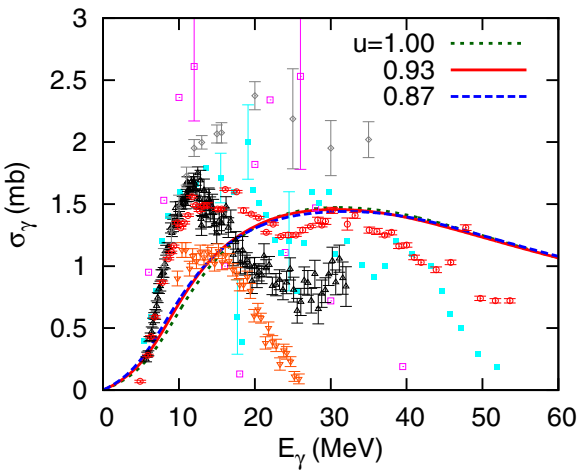

FIG. 6. Comparison of the photoabsorption cross sections of ^{6}Li. Experimental $^6\mathrm{Li}(\gamma, n)$ data are plotted as open rectangles [18], closed rectangles [43], open triangles [44], and inverted open triangles [45]. Since they are unavailable, most of error bars of the experimental data in Refs. [18,45] are not plotted. Diamonds are the cross sections taken from Ref. [46], where the contributions of the $h+t$ and $p+d+t$ channels are analyzed and taken into account. Open circles denote the $^6\mathrm{Li}(\gamma, n) + {}^6\mathrm{Li}(\gamma, 2n) + {}^6\mathrm{Li}(\gamma, 3n)$ data taken from Ref. [17].

decay width ∼40 MeV. Thus, we use the energy-dependent decay width that starts from the lowest threshold: $\Gamma(E) = [E - E(\alpha + d)] \tan 2\theta$, where $E(\alpha + d)$ is the $\alpha + d$ threshold energy. The θ value is determined to 27°, which reproduces the total sum of the cross sections of Ref. [17].

Figure 6 compares the calculated and experimental photoabsorption cross sections of ^{6}Li. Note that most of the experimental data are the cross sections for the $^6\mathrm{Li}(\gamma, n)$ reactions, and some channels, e.g., the $h+t$ and $p+d+t$ channels, are not taken into account in the data. Only the cross sections of Ref. [46] consider the $h+t$ and $p+d+t$ contributions. In the calculated total photoabsorption cross sections, only a single-peak structure is found. We remark that Refs. [12,13] also predicted a broad single-peak structure at around 20 MeV for the total photoabsorption cross sections of ^{6}Li with the six-body calculation, showing good agreement with the data [46]. One possible reason for the two-peak structure found in Ref. [17] could be that the contributions from the $h+t$ and $p+d+t$ channels are not included in the data [17]. In any case, the calculated results are almost identical for all u parameters due to large smearing width $\Gamma(E)$. Though all fine structures are smeared out, the cross-section values are quantitatively consistent with the measured cross sections, considering that the measured values are very scattered. For the quantitative comparison to the measured cross sections, it is necessary to describe the six-body continuum states appropriately with the aid of, e.g., the complex scaling method [47,48] and the Lorentz integral transform method [49], as well as the improvement of the nuclear interaction, although they are involved.

Let us compare the interpretation given in Refs. [17,18] and our findings. The measured cross sections of Ref. [17] show the two-peak structure and their interpretation on the two-peak structure was that the low-lying ($E_\gamma \lesssim 20$ MeV) peak comes from the typical GDR transition mode of ^{6}Li and the higher peak (from ∼30 to ∼40 MeV) corresponds to the GDR of the α cluster in ^{6}Li. Contrary to that interpretation, we see that the typical GDR or GT mode appears in the higher-lying energy regions around 35 MeV, where the α cluster is strongly distorted. In Ref. [18], the lower peak is interpreted as the disintegration to the $\alpha + p + n$ channels, whereas the higher peak is the GDR of ^{6}Li due to the disintegration of the α core. From the theoretical point of view, it is difficult to say whether this GDR mode is the GDR of the α cluster in ^{6}Li or not in the high-energy regions because they consist of identical fermions. In our interpretation, in the low-lying energy regions below the $h+t$ threshold (15.8 MeV), the soft GT-dipole transitions dominate the out-of-phase transition between the valence nucleons around the α cluster, which is consistent with the interpretation given in Ref. [18] for the lower-energy peak. This can be determined, as all the spectroscopic factors, $S^2_{\alpha pn}$, of the final states in this energy regions are almost unity. It is known that the excitation energy of the GDR is inversely proportional to the nuclear radius. According to the systematics of the GDR energy [41], this low-lying energy region corresponds to the GDR energies of $A \approx 200$ nuclei. Therefore, it is natural to interpret that the typical excitation mode in this energy region is the GT mode of the valence nucleons around the tightly bound α core, whereas the typical GDR mode of ^{6}Li suggested in Ref. [17] is unlikely, and we note that the ^{6}Li radius is about one half of the radii of the $A \approx 200$ nuclei [36]. In the intermediate energies from ∼20 to ∼30 MeV just between the low- and high-lying peaks of ^{6}Li, the prominent $h+t$ cluster GT-dipole mode appears, which is consistent with the interpretation given in Ref. [18] for the higher-energy peak. As summarized at the end of the previous subsection, the emergence of these various excitation modes can simply be recognized by the threshold energies, the Ikeda threshold rule [1].

D. Isoscalar dipole transitions

Here we discuss another operator to present more details on the transition densities. The compressive isoscalar dipole (IS1) operator [50] is defined by

$$\mathcal{M}(\mathrm{IS1}) = \sum_i (\boldsymbol{r}_i - \boldsymbol{x}_N)^2 \mathcal{Y}_{1\mu}(\boldsymbol{r}_i - \boldsymbol{x}_N). \tag{20}$$

The transition matrix of IS1 can be calculated by using the relation: $\int_0^\infty dr\, r^2(\rho_p^{\mathrm{tr}} + \rho_n^{\mathrm{tr}})$. The IS1 transitions have recently been intensively discussed because they are of particular importance to study the cluster structure (see recent theoretical and experimental papers [16,51,52] and references therein).

Figure 7 plots the IS1 strength distributions as a function of the excitation energies. We see some prominent strengths below 5 MeV having the isoscalar nature possibly by the $\alpha + d$ continuum, which cannot be excited by the $E1$ operator, which only has the isovector term. In fact, the $S^2_{\alpha d}$ values of those states are found to be almost unity and the transition densities of the state with the most prominent IS1 peak at $E_x = 3.3$ MeV shows in-phase transition in all regions.

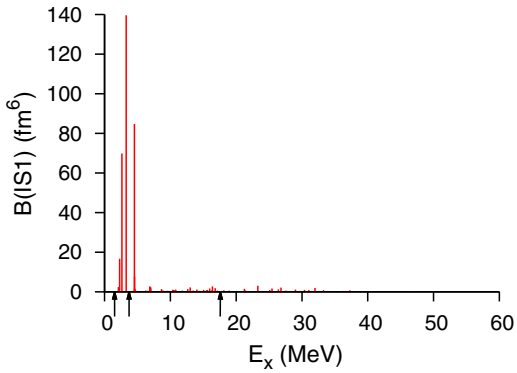

FIG. 7. Isoscalar dipole strengths of ^{6}Li as a function of the excitation energy. Arrows indicate the theoretical $\alpha + d$, $\alpha + p + n$, and $h + t$ thresholds from left to right, respectively.

Beyond 5 MeV, the IS1 strengths drop suddenly and very small strengths appear in the higher-energy regions. Most of the IS1 strengths are exhausted by the transitions to the $\alpha + d$ states below 5 MeV. In case of ^{6}He [14], since the low-lying soft-dipole mode is dominated by the surface excitation of the valence neutrons, several IS1 strengths appear at the low-lying regions. Contrary to the ^{6}He case, the states with all the prominent $E1$ strengths have the out-of-phase excitation character. The IS1 transition matrix, which is obtained by the sum of proton and neutron transition densities, is strongly canceled out in such excitation modes where the out-of-phase transitions dominate. The contributions from the in-phase transition regions in the soft GT-dipole mode become small in the IS1 strengths due to the additional r^2 factor appearing in the IS1 operator. The strong suppression of the IS1 transition strengths can be evidence that all the ^{6}Li final states beyond 5 MeV are dominated by the out-of-phase transitions. We remark that similar transition strengths are observed in the proton inelastic scattering on ^{6}Li [53], although a proton probe can excite both the isoscalar and isovector components. The experimental confirmation using an isoscalar probe such as an α particle is desired to clarify the excitation mechanism of ^{6}Li.

V. CONCLUSION

Motivated by the recent measurement of the photoabsorption cross sections of ^{6}Li [17], we have performed fully microscopic six-body calculations for the electric-dipole ($E1$) transition strengths. The ground-state wave function of ^{6}Li was obtained precisely by using the correlated Gaussian (CG) functions with the stochastic variational method. The final-state wave functions populated by the $E1$ operator were expanded by a number of the CG functions, including the explicit asymptotic cluster wave functions as well as their distorted configurations, which are important to describe the complicated six-nucleon dynamics. Emergence of various excitation modes has been found through the analysis of the transition densities from the ground- to final-state wave functions. The degrees of the clustering in those states have been quantified by evaluating the components of the $\alpha + p + n$ and $h + t$ clusters in the ^{6}Li wave functions to understand the role of these cluster configurations in the $E1$ excitations.

Nuclear clustering plays a crucial role in explaining the $E1$ excitation mechanism of ^{6}Li and its emergence strongly depends on the positions of the threshold energies. In the low-energy regions below the α breaking or $h + t$ threshold energy $\lesssim$16 MeV, we found that the $E1$ excitations are dominated by the "soft" dipole mode that exhibits the in-phase transitions of proton and neutron transition densities in the internal regions and the out-of-phase transitions beyond the nuclear surface. This can be interpreted as the out-of-phase oscillation between valence nucleons around the α cluster in ^{6}Li ("soft" GT-dipole mode), which is a very unique excitation mode. After the $h + t$ thresholds open, the $h + t$ cluster mode appears showing the out-of-phase transition in all regions and they also compete with the vibrational excitation of the soft GT-dipole modes having the $\alpha + p + n$ structure. Beyond 30 MeV, where all decay channels open, $\alpha + p + n$ and $h + t$ and other possible channels can mix and compete and, finally, the typical GDR mode appears in these energy regions.

These interpretations are different from the speculation given in Ref. [17] that the low-energy peak corresponds to the typical GDR of ^{6}Li. From the present analysis, we found that the $E1$ transition strengths of the ^{6}Li are dominated by the out-of-phase transitions of protons and neutrons in the surface regions from the low- to high-energy regions, which is in contrast to ^{6}He where the neutron transition dominates at the low-energy regions. This phase property can be verified by using an isoscaler probe such as an α inelastic-scattering measurement to confirm whether no prominent strength is found after the $\alpha + p + n$ threshold.

It is interesting to explore whether the soft GT mode appears in the low-lying energy regions of heavier nuclei. Since the excitation mode emerges from the out-of-phase transition of the proton and neutron of the d-cluster around the core in the initial ground-state wave function, the ground-state wave function should have a well-developed core plus d-cluster structure. The most probable candidate is ^{18}F because the ground-state spin-parity is 1^+ like ^{6}Li and a $^{16}\mathrm{O} + p + n$ cluster structure component can be large.

Also, as a natural extension of ^{6}Li, a nucleus ^{7}Li is worth studying [17]. Since the $\alpha + t$ threshold is the lowest (2.47 MeV), the cluster GT mode of $\alpha + t$ is expected to appear first, and then the other excitation modes appear with respect to the opening of the particle decay channels $\alpha + d + p$, $\alpha + p + p + n$, $t + h + n$, etc., in order.

These studies will serve as the universal understanding of the emergence of the nuclear clustering and reveal the excitation mechanism of nuclei through the $E1$ field, which is one of the simplest probes of the nuclear structure.

ACKNOWLEDGMENTS

The authors thank J. Singh for a careful reading of the manuscript. This work was in part supported by JSPS KAKENHI Grants No. 18K03635, No. 18H04569, and No. 19H05140, and the collaborative research program 2019, information initiative center, Hokkaido University.

APPENDIX A: CALCULATION OF THE SPECTROSCOPIC FACTORS

As a measure of degrees of the clustering, we evaluate the spectroscopic factors, which are the components of finding the α, $\alpha + d$, and $h + t$ configurations in the wave function of ^{6}Li. Equations (16) and (9) are respectively written more explicitly as

$$S^2_{\alpha pn} = \left| \iint d\boldsymbol{r}\, d\boldsymbol{r}' \langle \Psi^{(\alpha)} \Psi^{(p)} \Psi^{(n)} | \times \delta(\boldsymbol{y}_1 - \boldsymbol{r}) \delta(\boldsymbol{y}_2 - \boldsymbol{r}') \left| \Psi^{(6)}_{JM_J}(E) \right\rangle \right|^2, \quad \text{(A1)}$$

$$S^2_{ht} = \left| \int d\boldsymbol{r} \left\langle \Psi^{(h)} \Psi^{(t)} \delta(\boldsymbol{z} - \boldsymbol{r}) \right| \Psi^{(6)}_{JM_J}(E) \right\rangle \right|^2. \quad \text{(A2)}$$

All the relative wave functions are integrated out by using the orthonormal basis $\sum_{lm} \phi_{l,i}(r) Y_{lm}(\hat{\boldsymbol{r}})$ constructed from a sufficient number of Gaussian functions, $r^l \exp(-ar^2)$, as a complete set. Practically, we make the orthonormal basis sets by diagonalizing the relative wave functions used in the final-state wave function of types (II) and (III). More explicitly, we diagonalize the following overlap matrices using the coefficients of the bases that give the ground-state wave function of a nucleus x, $C^{(x)}_i$ for the $\alpha + p + n$ spectroscopic factor,

$$B^{(\alpha pn)}_{mn} = \sum_{i,j}^{K_4} C^{(\alpha)}_i C^{(\alpha)}_j \left\langle \Phi^{(411,k)}_{JM_J,im} \middle| \Phi^{(411,l)}_{JM_J,jn} \right\rangle \quad \text{(A3)}$$

with k and l run for 1 and 2 corresponding to the Y and T types, respectively. We take $K_4 = 15$. In the end, the dimension of $B^{(\alpha pn)}$ is 1080. For the $h + t$ spectroscopic factors, we diagonalize the following overlap matrix:

$$B^{(ht)}_{mn} = \sum_{i,j,k,l}^{K_3} C^{(h)}_i C^{(t)}_j C^{(h)}_k C^{(t)}_l \left\langle \Phi^{(33)}_{JM_J,ijm} \middle| \Phi^{(33)}_{JM_J,kln} \right\rangle \quad \text{(A4)}$$

with $K_3 = 7$. Finally, all the spectroscopic factors calculated in this paper are evaluated by the overlap matrix element of the correlated Gaussians [25,28]. The same procedure is applied for the evaluation of the $\alpha + d$ spectroscopic factor as well.

APPENDIX B: ELECTRIC-DIPOLE TRANSITIONS ONLY WITH $\alpha + p + n$ AND $h + t$ CONFIGURATIONS

Here we discuss the $E1$ transitions only with the $\alpha + p + n$ and $h + t$ configurations, which are respectively constructed by the diagonalization of the following basis functions:

$$\Phi^{(\alpha pn),m}_{JM_J,jk} = \sum_i C^{(\alpha)}_i \Phi^{(411,m)}_{JM_J,ijk}, \quad \text{(B1)}$$

$$\Phi^{(ht)}_{JM_J,k} = \sum_{i,j} C^{(h)}_i C^{(t)}_j \Phi^{(33)}_{JM_J,ijk}, \quad \text{(B2)}$$

where $C^{(x)}_i$ are a set of the coefficients that give the ground-state wave function of a cluster $x (= h, t,$ and $\alpha)$. Figure 8 plots the transition strengths only with the $\alpha + p + n$ and $h + t$ final-state configurations. As expected the transition strengths only with the $\alpha + p + n$ configurations below 30 MeV are similar to the results displayed in Fig. 4(a) where the $S^2_{\alpha pn}$ values are large. We only find three significant strengths with the $h + t$ configurations and the positions of the two lowest prominent peaks at $E_x = 20.0$ and 23.9 MeV remain unchanged with the full model space calculations, while the most prominent peak at $E_x = 36.4$ MeV split into small strengths in the full model space calculation as shown in Fig. 3(b). We find the state has relatively large square overlap with the $\alpha + p + n$ configuration (0.281), leading to level splitting due to channel coupling.

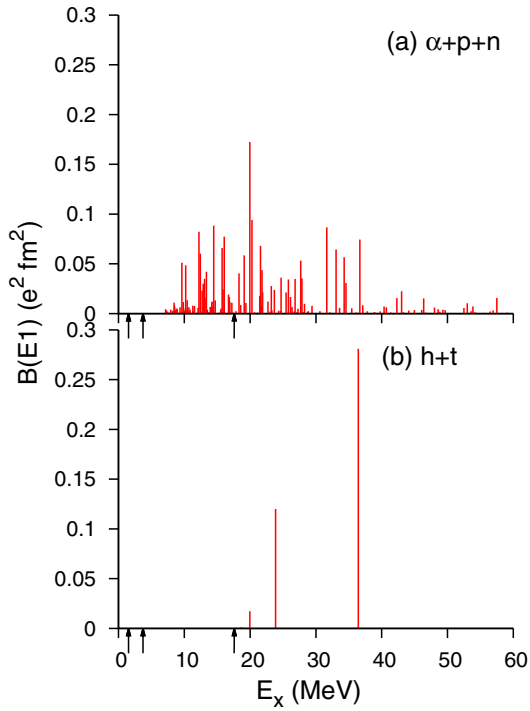

FIG. 8. Electric-dipole strengths only with (a) $\alpha + p + n$ and (b) $h + t$ final-state configurations. Arrows indicate the theoretical $\alpha + d$, $\alpha + p + n$, and $h + t$ thresholds from left to right, respectively.

We calculate the transition densities with the $\alpha + p + n$ configuration that give the three largest $B(E1)$ strengths for each configuration and are shown in Figs. 9(a), 9(c), and 9(e). These almost explain the characteristic behaviors of the transition densities of the states with large $S^2_{\alpha pn}$, which are the soft GT-dipole modes. All the transition densities have in-phase transitions inside, around the nuclear radius, and out-of-phase transitions beyond the surface. It is interesting to note the nodal or oscillatory behavior in the in-phase regions of the transition densities around the radius of the α particle. This is due to the Pauli principle between the core and valence nucleon. As we see in the transition densities of ^{6}He, the nodal behavior of the transition density can only be seen in the neutron transition [14].

We also plot, in the Figs. 9(b) and 9(d), the transition densities only with the $h + t$ configurations for the states giving the two highest $E1$ strengths. They show typical GDR behavior and peak positions are at around the nuclear surface, which explains the behavior of the transition densities of Figs. 5(b) and 5(d). In this restricted model space, we do not obtain the

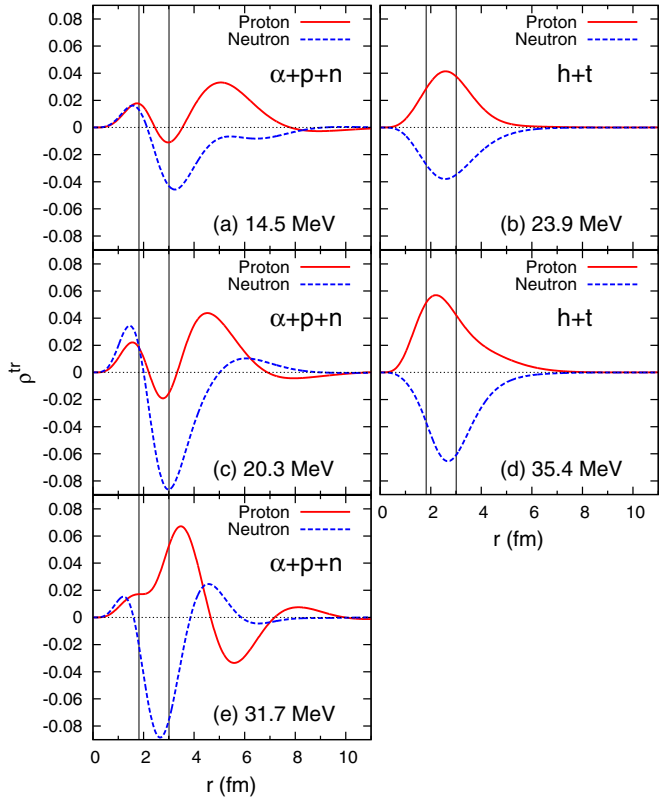

FIG. 9. Transition densities to the states that give the prominent $E1$ strength only with the restricted model spaces: The $\alpha + p + n$ final-state configurations at (a) $E_x = 14.5$, (c) 20.3, and (e) 31.7 MeV, and the $h + t$ final-state configurations at (b) $E_x = 23.9$ and (d) 35.4 MeV. See the text for details. Vertical thin lines indicate theoretical nuclear radii, $\sqrt{\frac{5}{3}}r_m$, of ^{4}He and ^{6}Li, respectively.

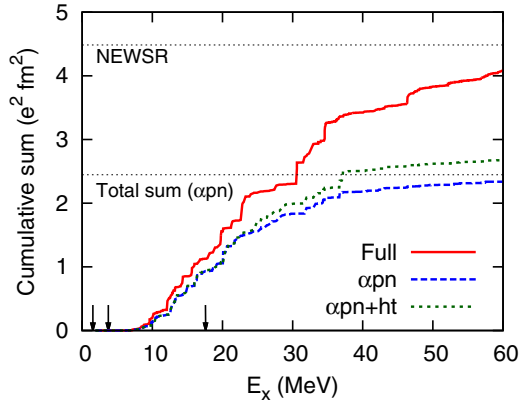

FIG. 10. Cumulative sum of the $E1$ transition strengths of ^{6}Li with the full model space, $\alpha + p + n$, and $(\alpha + p + n) + (h + t)$ configurations with $u = 0.93$. The NEWSR value and the total sum of the $E1$ strengths only with the $\alpha + p + n$ configurations are plotted as thin dotted lines for comparison. See text for details. Arrows indicate the theoretical $\alpha + d$, $\alpha + p + n$, and $h + t$ thresholds from left to right, respectively.

similar transition densities to the state with $E_x = 34.6$ MeV, implying that these clusters are strongly distorted, as was shown in the GDR mode at $E_x = 32.9$ MeV in ^{6}He [14].

APPENDIX C: NON-ENERGY WEIGHTED SUM RULE

Here we discuss the impact of the clustering configurations on the $E1$ sum rule. The non-energy-weighted sum rule (NEWSR) can be evaluated by

$$\sum_{E_f} B(E1, E_f) = e^2\left[Z^2 r_p^2 - \frac{Z(Z-1)}{2} r_{pp}^2\right]. \qquad \text{(C1)}$$

We obtain 4.49 e^2 fm^2 as a total sum of the $E1$ transition strengths with the full model space. The NEWSR is fully satisfied, that is, 99.6% of the right-hand side of Eq. (C1) is fulfilled in the present model space. To quantify the importance of the α clustering, we calculate the left-hand-side equation only with the $\alpha + p + n$ configuration defined in Eq. (B1) and the value is 2.45 e^2 fm^2, satisfying 55% of the total sum-rule value.

Figure 10 compares the cumulative sum of ^{6}Li of the $E1$ strengths with the full model space as well as the ones only with the $\alpha + p + n$ configurations. To get the sum rule satisfied, say, 80%, the cumulative sum with the full model space needs to integrate up to about 45 MeV, whereas the most of the important configurations with the $\alpha + p + n$ configuration are exhausted at 33 MeV where its cumulative sum exceeds 80% of its total sum. We find that the configurations other than the $\alpha + p + n$ configurations are also important in such low-lying regions below ∼20 MeV and even the $h + t$ threshold does not open. They are used to describe the polarization of the clusters through the coupling of those cluster configurations. The difference between the cumulative sum of the full model space and $\alpha + p + n$ are 30% at 10 MeV and the difference becomes large as the incident energy increases. We also display in Fig. 10 the cumulative sum of the transition strengths with the mixing of $\alpha + p + n$ and $h + t$ configurations defined respectively in Eqs. (B1) and (B2). The $h + t$ configurations play a role beyond ∼20 MeV after opening the $h + t$ threshold and improve the NEWSR value by 8%. However, it is not enough to explain all the needed configurations included in the strengths with the full model space. In the higher energies, the breaking of these cluster configurations becomes more important as various configurations can contribute to the $E1$ transitions.

[1] K. Ikeda, N. Takigawa, and H. Horiuchi, Prog. Theor. Phys. Suppl. **E68**, 464 (1968).

[2] Y. Fujiwara, H. Horiuchi, K. Ikeda, M. Kamimura, K. Katō, Y. Suzuki, and E. Uegaki, Prog. Theor. Phys. Suppl. **68**, 29 (1980).

[3] F. Hoyle, Astrophys. J. Suppl. Ser. **1**, 121 (1954).
[4] M. Goldhaber and E. Teller, Phys. Rev. **74**, 1046 (1948).
[5] H. Steinwedel and J. H. D. Jensen, Z. Naturforsch. **5a**, 413 (1950).
[6] C. J. Horowitz and J. Piekarewicz, Phys. Rev. Lett. **86**, 5647 (2001).
[7] A. Tamii, I. Poltoratska, P. von Neumann-Cosel, Y. Fujita, T. Adachi, C. A. Bertulani, J. Carter, M. Dozono, H. Fujita *et al.*, Phys. Rev. Lett. **107**, 062502 (2011).
[8] P. G. Hansen and B. Jonson, Europhys. Lett. **4**, 409 (1987).
[9] T. Yamazaki *et al.*, A Draft Proposal for Japanese Hadron Project, p. 59 (1987) [in Japanese].
[10] K. Ikeda, INS Report No. JHP-7 (1988) [in Japanese].
[11] Y. Suzuki, K. Ikeda, and H. Sato, Prog. Theor. Phys. **83**, 180 (1990).
[12] S. Bacca, M. A. Marchisio, N. Barnea, W. Leidemann, and G. Orlandini, Phys. Rev. Lett. **89**, 052502 (2002).
[13] S. Bacca, N. Barnea, W. Leidemann, and G. Orlandini, Phys. Rev. C **69**, 057001 (2004).
[14] D. Mikami, W. Horiuchi, and Y. Suzuki, Phys. Rev. C **89**, 064303 (2014).
[15] T. Inakura, W. Horiuchi, Y. Suzuki, and T. Nakatsukasa, Phys. Rev. C **89**, 064316 (2014).
[16] Y. Kanada-En'yo and Y. Shikata, Phys. Rev. C **95**, 064319 (2017).
[17] T. Yamagata, S. Nakayama, H. Akimune, and S. Miyamoto, Phys. Rev. C **95**, 044307 (2017).
[18] S. Costa, S. Ferroni, W. Wataghin, and R. Malvano, Phys. Lett. **4**, 308 (1963).
[19] A. Csótó and R. G. Lovas, Phys. Rev. C **46**, 576 (1992).
[20] M. V. Zhukov, B. V. Danilin, D. V. Fedorov, J. M. Bang, I. J. Thompson, and J. S. Vaagen, Phys. Rep. **231**, 151 (1993).
[21] W. Horiuchi and Y. Suzuki, Phys. Rev. C **76**, 024311 (2007).
[22] S. Watanabe, T. Matsumoto, K. Ogata, and M. Yahiro, Phys. Rev. C **92**, 044611 (2015).
[23] D. R. Thompson, M. LeMere, and Y. C. Tang, Nucl. Phys. A **286**, 53 (1977).
[24] K. Varga and Y. Suzuki, Phys. Rev. C **52**, 2885 (1995).
[25] Y. Suzuki, W. Horiuchi, M. Orabi, and K. Arai, Few-Body Syst. **42**, 33 (2008).
[26] V. D. Efros, W. Leidemann, G. Orlandini, and E. L. Tomusiak, Phys. Lett. B **484**, 223 (2000).
[27] D. Gazit, S. Bacca, N. Barnea, W. Leidemann, and G. Orlandini, Phys. Rev. Lett. **96**, 112301 (2006).
[28] Y. Suzuki and K. Varga, *Stochastic Variational Approach to Quantum-Mechanical Few-Body Problems*, Lecture Notes in Physics (Springer, Berlin, 1998), Vol. m54.
[29] Y. Suzuki, J. Usukura, and K. Varga, J. Phys. B: At. Mol. Opt. Phys. **31**, 31 (1998).
[30] W. Horiuchi and Y. Suzuki, Phys. Rev. C **78**, 034305 (2008).
[31] W. Horiuchi and Y. Suzuki, Phys. Rev. C **89**, 011304(R) (2014).
[32] S. Ohnishi, W. Horiuchi, T. Hoshino, K. Miyahara, and T. Hyodo, Phys. Rev. C **95**, 065202 (2017).
[33] J. Mitroy, S. Bubin, W. Horiuchi, Y. Suzuki, L. Adamowicz, W. Cencek, K. Szalewicz, J. Komasa, D. Blume, and K. Varga, Rev. Mod. Phys. **85**, 693 (2013).
[34] Y. Suzuki and W. Horiuchi, *Emergent Phenomena in Atomic Nuclei from Large-scale Modeling: A Symmetry-Guided Perspective* (World Scientific, Singapore, 2017), Chap. 7, pp. 199–227.
[35] D. R. Tilley, C. M. Cheves, J. L. Godwin, G. M. Hale, H. M. Hofmann *et al.*, Nucl. Phys. A **708**, 3 (2002).
[36] I. Angeli and K. P. Marinova, At. Data Nucl. Data Tables **99**, 69 (2013).
[37] N. Kawamura and W. Horiuchi, *Springer Proceedings in Physics* (Springer, Berlin, in press).
[38] J. L. Forest, V. R. Pandharipande, S. C. Pieper, R. B. Wiringa, R. Schiavilla, and A. Arriaga, Phys. Rev. C **54**, 646 (1996).
[39] W. Horiuchi, Y. Suzuki, and K. Arai, Phys. Rev. C **85**, 054002 (2012).
[40] W. Horiuchi and Y. Suzuki, Phys. Rev. C **87**, 034001 (2013).
[41] P. Ring and P. Schuck, *The Nuclear Many-Body Problem*, Texts and Monographs in Physics (Springer, Berlin, 1980).
[42] E. C. Pinilla, D. Baye, P. Descouvemont, W. Horiuchi, and Y. Suzuki, Nucl. Phys. A **865**, 43 (2011).
[43] E. B. Bazhanov, A. P. Komar, and A. V. Kulikov, Nucl. Phys. **68**, 191 (1965).
[44] B. L. Berman, R. L. Bramblett, J. T. Cadwell, R. R. Harvey, and S. C. Fultz, Phys. Rev. Lett. **15**, 727 (1965).
[45] V. P. Denisov, A. P. Komar, L. A. Kul'chiskiy, and E. D. Makhnovskiy, Yad. Fiz. **5**, 498 (1967).
[46] W. A. Wurtz, R. E. Pywell, B. E. Norum, S. Kucuker, B. D. Sawatzky, H. R. Weller, S. Stave, and M. W. Ahmed, Phys. Rev. C **90**, 014613 (2014).
[47] N. Moiseyev, Phys. Rep. **302**, 212 (1998).
[48] S. Aoyama, T. Myo, K. Katō, and K. Ikeda, Prog. Theor. Phys. **116**, 1 (2006).
[49] V. D. Efros, W. Leidemann, G. Orlandini, and N. Barnea, J. Phys. G **34**, R459 (2007).
[50] S. Stringari, Phys. Lett. B **108**, 232 (1982).
[51] Y. Chiba, Y. Taniguchi, and M. Kimura, Phys. Rev. C **95**, 044328 (2017).
[52] S. Adachi, T. Kawabata, K. Minomo, T. Kadoya, N. Yokota, H. Akimune, T. Baba, H. Fujimura, M. Fujiwara *et al.*, Phys. Rev. C **97**, 014601 (2018).
[53] T. Yamagata, N. Warashina, H. Akimune, S. Asaji, M. Fujiwara, M. B. Greenfield, H. Hashimoto, R. Hayami, T. Ishida *et al.*, Phys. Rev. C **74**, 014309 (2006).